Research Paper

CuInS$_2$ quantum dots embedded in Bi$_2$WO$_6$ nanoflowers for enhanced visible light photocatalytic removal of contaminants

Sheng Luo[a], Jun Ke[a,b,*], Mengqian Yuan[a], Qi Zhang[a], Peng Xie[a], Lidan Deng[a], Shaobin Wang[b,*]

[a] School of Chemistry and Environmental Engineering, Wuhan Institute of Technology, Wuhan 430073, China
[b] Department of Chemical Engineering, Curtin University, GPO Box U1987, Perth, WA 6845, Australia

ABSTRACT

Novel CuInS$_2$ quantum dots (CIS-QDs)/Bi$_2$WO$_6$ 3D composites were successfully synthesized through a facile deposition process, followed by low temperature calcination. The ternary p-type CIS-QDs were highly dispersed onto the surface of flower-like n-type Bi$_2$WO$_6$ nanosheets to form *p-n* heterojunction and simultaneously tune the behaviors of photogenerated charge carriers, resulting in higher photocatalytic efficiencies of toluene degradation and Cr(VI) reduction under visible light irradiation, which are 3.0 and 8.5 times higher than those of Bi$_2$WO$_6$, respectively. The photoelectrochemical investigations indicate that the introduction of CIS-QDs synergistically enhanced the harvesting efficiency of solar energy in the *p-n* heterojunction system with the internal electric field and reduced transfer barrier of photoinduced charge carriers by forming the unique Bi−S bonds between the CIS-QDs and flower-like Bi$_2$WO$_6$.

1. Introduction

Volatile organic compounds (VOCs) are considered as a major group of air pollutants, commonly including toluene, xylene, and formaldehyde, which cause severe deterioration of air quality and have toxicity and carcinogenicity to humans [1,2]. In the past, a series of conventional techniques, for example catalytic combustion, have been developed to eliminate VOCs in the industrial fields [3–5]. Nevertheless, there are some demerits involved in the degradation process, such as low removal efficiency for trace VOCs, production of various secondary pollutants, and high consumption temperature [6]. Therefore, there is a great demand to develop a more cost-effective, more efficient and environmentally benign technology for removal of indoor VOCs at a low concentration.

Heterogeneous photocatalytic oxidation is viewed as a promising technology for removal of organic pollutants, because these organic pollutants can be oxidized to CO$_2$ and H$_2$O at room temperature in the presence of photocatalysts [7–10]. Bismuth tungstate (Bi$_2$WO$_6$) stands out among many attractive candidate materials because of its unique properties, such as a suitable band gap of 2.75 eV, and good photostability. More importantly, as a layered Aurivillius-related oxide semiconductor, it is composed of accumulated layers of corner-sharing [WO$_6$] octahedral sheets and [Bi$_2$O$_2$] layers [11]. On the other hand, the conduction band (CB) of Bi$_2$WO$_6$ is comprised of W 5d orbitals; whereas its valence band (VB) is mainly formed by hybridizing O 2p with Bi 6 s orbitals [12], which not only makes the valence band largely dispersed, but also favors the mobility of photo-induced holes for specific oxidation reactions, such as organic synthesis, water oxidation, and pollutant decomposition [13–16]. However, similar to many other semiconductors, the poor harvesting of solar energy and charge carrier separation of pure Bi$_2$WO$_6$ lead to the low photocatalytic activity and thus it cannot meet the demand of commercial applications.

In contrast to single component photocatalysts, heterojunction photocatalysts that combine at least two functional materials in one system have received more attention in the past decades [17–19]. Among advanced heterojunction materials, owing to unique quantum effect and high optical absorption, quantum dots (QDs) are often utilized as a visible light sensitizer to tune behaviors of photogenerated charge carriers in composites, which could influence and adjust the electronic and optical behaviors of the original composition [20–25]. Among numerous semiconductor QDs, copper indium disulfide (CuInS$_2$) is a direct I-III-VI band gap semiconductor with a bulk band gap of 1.5 eV, and possesses a high optical coefficient in the visible spectral range (10^5 cm^{-1}), chemical stability, and less toxicity [26–28]. More importantly, there are abundant defects located on the surface of CuInS$_2$ QDs, which are the nonradiative recombination sites of the carriers and beneficial for efficiently accelerating reaction on the surface of the catalysts. Therefore, it is interesting to develop a heterojunction photocatalyst by manipulating the interactions between CuInS$_2$ QDs and Bi$_2$WO$_6$ photocatalysts for efficiently increasing

* Corresponding authors at: Department of Chemical Engineering, Curtin University, GPO Box U1987, Perth, WA 6845, Australia.
  E-mail addresses: kejunmars@hotmail.com (J. Ke), shaobin.wang@curtin.edu.au (S. Wang).

photocatalysis under visible light irradiation.

Based on the above strategies, in this study, $CuInS_2$ QDs (CIS-QDs) and hierarchical Bi_2WO_6 (BWO) were separately prepared through solvent thermal methods and then coupled together by low temperature annealing to form CIS-BWO heterojunction for improving efficiency of solar energy utilization and photoinduced charge transportation. The heterojunction system displayed an enhanced photocatalytic ability for gaseous toluene decomposition and aqueous toxic Cr(VI) reduction under visible light irradiation. Moreover, the photoelectrochemical properties were investigated to probe the charge transportation behavior. It is evidently observed that the introduction of CIS-QDs and formation of Bi−S bonds between the CIS-QDs and Bi_2WO_6 plays an important role in enhancing the harvesting efficiency of solar energy in the heterojunction, reducing transportation barrier of charge carrier, and thus improving photocatalytic ability, which could provide deep insights into design and application of excellent photocatalysts in the future.

2. Experimental section

2.1. Synthesis of CIS-QDs

CIS-QDs were synthesized in a noncoordinating 1-octadecene solvent. In a typical case, 0.2 mmol CuCl and 0.2 mmol $InCl_3·4H_2O$ were mixed with 2 mL of 1-dodecanethiol and 12 mL of 1-octadecene in a three-neck flask. The mixture solution was stirred under a primary vacuum for 5 min, backfilled with nitrogen for 15 min, and then heated to 353 K under a vacuum for 5 min. After that, under nitrogen atmosphere, the above mixture was heated to 373 K for 15 min, and then to the reaction temperature of 493 K. After keeping the mixture at the reaction temperature for 120 min under the flow of nitrogen, the quantum dots were dispersed in chloroform and precipitating with ethanol, and centrifuging. The dispersion/precipitation cycle was repeated thrice, and then the CIS-QDs were dispersed in 2 mL of chloroform solution.

2.2. Synthesis of Bi_2WO_6 nanoflowers

Flower-like Bi_2WO_6 was synthesized by a facile hydrothermal method. In details, 0.98 g of $Bi(NO_3)_3·5H_2O$ was dissolved in 40 mL of 0.3 M HNO_3 *via* ultrasonication. Then, 20 mL of 0.05 M $Na_2WO_4·2H_2O$ solution was added with vigorous stirring and a white precipitate was formed. After that, 20 mL of 0.2 M NaOH solution was added dropwise and the mixture was kept stirring for 24 h. Then, the mixture was transferred to a Teflon-lined autoclave and maintained at 433 K for 8 h. The obtained suspension was cooled down to room temperature, centrifuged, washed by purified water and dried in air at 333 K, named as BWO.

2.3. Construction of CIS-QDs/BWO photocatalysts

Different amounts of CIS-QDs were ultrasonically dispersed in 4 mL of chloroform solution and then BWO powder was added under vigorous stirring. The above mixture was kept stirring at 313 K until the solvent was completely volatilized. After that, the CIS-QDs/Bi_2WO_6 heterojunction photocatalyst was obtained by annealing the mixture at 473 K for 15 min. Several CIS-QDs/BWO samples at different mass ratios of CIS QDs (0.1%, 1%, and 3%) were prepared by changing the amounts of CIS-QDs chloroform solution and were denoted as 0.1%CIS-BWO, 1%CIS-BWO, and 3%CIS-BWO, respectively.

2.4. Characterizations

X-ray powder diffraction (XRD) was carried out on a Bruker axs D8 Discover (Cu Kα = 1.5406 Å). Scanning electron microscopy (SEM) images were taken on a Hitachi S4800 scanning electron microscope

operating at 5.0 kV. Transmission electron microscopy (TEM, JEOL JEM2100) was operated at 200 kV. The UV–vis absorption spectra were recorded on a MAPADA UV 6100. The Fourier transform infrared (FTIR) and Raman spectra were collected on the Bruker TENSOR 27 and Laser Confocal Microscopy Raman Spectrometer (Thermo Fisher Scientific, DXR), respectively. UV–vis diffuse reflectance spectra (DRS) were recorded on a UV–vis spectrophotometer (HITACHI UH4150) by using $BaSO_4$ as a reference and were converted from reflection to absorbance by the Kubelka-Munk method. Room-temperature photoluminescence spectra were detected with a Hitachi fluorescence spectrophotometer (Hitachi F4600). The luminescence decay curve was obtained from FLS920 and the excitation source was a 350 W Xenon lamp. The Brunauer-Emmett-Teller (BET) specific surface area of the powders was analyzed by nitrogen adsorption on a Micromeritics ASAP 2020 nitrogen adsorption apparatus (USA). X-ray photoelectron spectroscopy (XPS) was performed on a VG Multilab 2000 (VG Inc.) photoelectron spectrometer using Al Kα radiation as the excitation source under vacuum at 2×10^{-6} Pa. All the binding energy (BE) values were calibrated by the C 1 s peak at 284.6 eV of the surface adventitious carbon.

2.5. Photoelectrochemical experiments

The photoelectrochemical tests were performed on a CHI660E electrochemistry workstation (Chenhua, Shanghai, China) at room temperature. All the experiments were carried out in a standard three-electrode cell containing 0.5 M Na_2SO_4 aqueous solution with platinum foil and a saturated calomel electrode (SCE) as the counter electrode and the reference electrode, respectively. To prepare working electrodes, an Indium-Tin Oxide (ITO) conductive film glass was ultrasonically cleaned in soap suds, deionized water, and acetone, successively. The electrodes were prepared by dropwise adding a slurry containing 80% of the as-prepared photocatalysts, 10% dimethylformamide (DMF), and 10% Nafion onto the ITO glass and then dried in air at 333 K for 6 h. The area of the electrodes is about 1×1 cm^2. A 500 W Xe lamp with a 420 nm cutoff filter was used as the light source.

2.6. Photocatalytic activity evaluation

The photooxidation of toluene under visible light irradiation was performed in a 120 mL homebuilt quartz photoreaction cell equipped with two KBr windows and a sample holder (diameter, 13 mm) for the catalyst wafer (0.2 g). The reaction atmosphere was air at a relative humidity of 45%, and the reaction temperature was about 293 K. After the catalyst was placed in the sample holder, a small amount of toluene (1 μL) was injected into the reactor with a microsyringe. When the photocatalyst sample reached adsorption equilibrium in the reactor after 1 h, a Xenon lamp (XQ-500W) with a 420 nm UV-cutoff filter was turned on. The IR spectra were continuously collected on the Bruker TENSOR 27 with a resolution of 1 cm^{-1} and 32 scans in the region of 4000-400 cm^{-1} during the reaction. The concentrations of toluene were analyzed by a gas chromatograph (Fuli 9720) equipped with a FID (KB-FFAP capillary column, 30 m × 0.32 mm × 1 μm). The amount of CO_2 was also determined by the Fuli 9720 gas chromatograph equipped with a thermal conductivity detector.

The aqueous photocatalytic reduction of Cr(VI) over the samples were evaluated under visible light irradiation by using a 500 W Xe lamp with a 420 nm cut-off filter (Beijing CEAULIGHT). In a typical photocatalytic procedure, 0.02 g of photocatalyst was added into 40 mL of Cr(VI) solution (10 mg/L). The suspensions were stirred in dark for 30 min to reach an adsorption-desorption equilibrium before illumination. Then, the solution was exposed to light irradiation under magnetic stirring. At each given time interval, 3 mL suspension was sampled and centrifuged to remove the solid. The concentration of Cr(VI) during the reduction was monitored by colorimetry using a
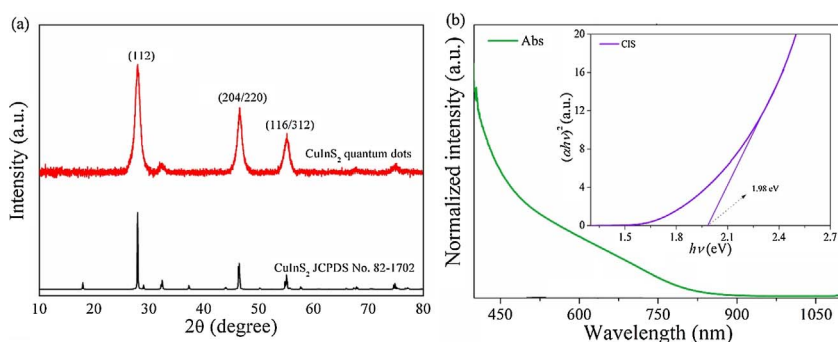
Fig. 1. XRD patterns (a), and UV–vis absorption spectrum (b) of the as-prepared CIS-QDs. The inset is the Tauc's curves.

MAPADA UV6100S spectrophotometer. The measurements were carried out at room temperature.

3. Results and discussion

XRD pattern of the as-prepared CIS-QDs is shown in Fig. 1a, where the major diffraction peaks at 28.08°, 46.63°, and 55.23° can be well indexed to the (112), (220)/(214), and (116)/(312) facets of the chalcopyrite crystal structure of $CuInS_2$ (JCPDS No. 82-1702), respectively [29]. Meanwhile, there are no observable diffraction peaks of impurities in the XRD pattern, such as CuS, Cu_2S, or In_2S_3. The absorption spectrum of the CIS-QDs (Fig. 1b) showed a broad shoulder with a tail in the long wavelength direction, which is the characteristic broad absorption spectra of ternary quantum dots [26]. The CIS-QDs displays an sharp absorption increase at 625 nm, where the size of the CIS-QDs is 5.3 nm estimated by the reported empirical equation [30,31]. Based on the previous report [27], E_g of the as-prepared CIS QDs as a direct transition semiconductor was estimated by the empirical equation of the Tauc's plots, $(\alpha h\nu)^2 = A(h\nu - E_g)$, where α, ν, E_g and A are the absorption coefficient, light frequency, bandgap energy and a constant, respectively. The calculated band gap energy (E_g) of the CIS-QDs is equal to 1.98 eV (the inset in Fig. 1b), suggesting a significant quantum confinement effect and benefit for exposing the abundant defects and dangling bonds on the surface by providing more active sites for photocatalytic reaction [32].

CIS-QDs/BWO heterojunction composites were prepared through coupling the CIS-QDs with hierarchical Bi_2WO_6. As shown in Fig. 2, XRD patterns of the as-prepared samples present good crystallinity and the distinct diffraction peaks are indexed to the orthorhombic Bi_2WO_6 phase (JCPDS No. 73-1126) [33,34]. Meanwhile, it was clearly observed that the CIS-BWO composites retained the crystalline structure of the pristine BWO, indicating that the thermal treatment process did not cause any change in crystal structure. Owing to the low amount and
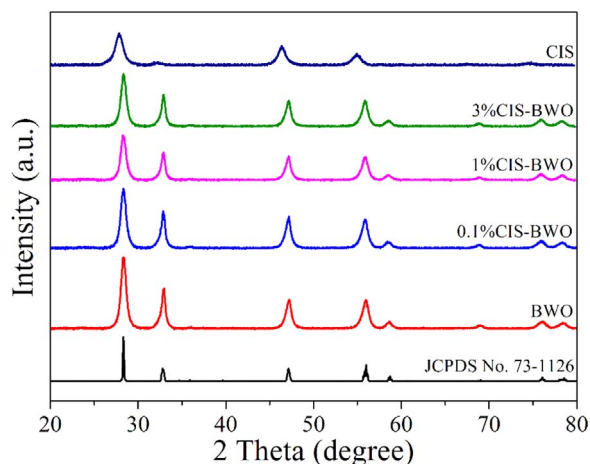
relative low diffraction intensity of CIS-QDs, the distinct diffraction peaks corresponding to the CIS-QDs were not observed, which is agreement with the previous reports [35,36].

To verify the composition and structure of the samples, the pristine BWO and 1%CIS-BWO samples were investigated by transmission electron microscopy (TEM), as shown in Fig. 3. It is found that the as-prepared QDs are nearly mono-dispersion with an average diameter of about 5 nm in Fig. 3a. Both of the pristine BWO and CIS-QDs/BWO samples display spherical particles with hierarchical structures and have a relatively uniform size (Fig. 3b and c). After coupling the CIS-QDs and BWO, as shown in Fig. 3d, a plenty of CIS-QDs were anchored on the surface of BWO uniformly. In addition, in Fig. 3e, the observed lattice fringes of 0.319 nm and 0.821 nm correspond to the (112) plane of chalcopyrite $CuInS_2$ and the (002) plane of orthorhombic Bi_2WO_6, respectively [37,38]. Meanwhile, the distinct borderline at the interface between CIS-QDs and BWO demonstrated that the CIS-QDs were closely dispersed on the surface of BWO with no buffer layers or amorphous phase in Fig. 3f, indicating the formation of heterojunction in the composites. Moreover, the element distribution at the interface was analyzed by the EDS linear scan method, as shown in Fig. S1. In the spectrum, the characteristic peaks assigned to Cu, In, S, Bi, W, and O elements were observed in the interface, which confirms that the CIS-QDs and BWO closely contact together and form the heterojunction.

To further visualize the morphology and structure of the samples, SEM images of BWO and 1%CIS-BWO samples were displayed in Fig. 4. It is apparently observed that both the BWO and 1%CIS-BWO samples possess uniform flower-like hierarchical structures with diameters ranging from 2 to 3 μm, which demonstrates that the low temperature thermal treatment hardly damaged the origin hierarchical structure of BWO. Furthermore, all the as-prepared samples present similar nitrogen adsorption/desorption isotherm and pore size distribution curves, as shown in Fig. S2. These curves display type-IV adsorption/desorption isotherms with H3 hysteresis loops, which are typical characteristics of porous materials [39]. The surface areas of BWO, 0.1%CIS-BWO, 1%CIS-BWO, and 3%CIS-BWO were calculated to be 32.9, 35.5, 33.1, and 27.4 m^2/g, respectively, which indicates that the introduction of the CIS-QDs could to some degree enlarge the specific surface area of the BWO and facilitate to improve photocatalytic performance of the heterojunction system. In contrast, when the amount of QDs are excessive, the pores of BWO were filled and blocked by the nanosized QDs, leading to a decreased surface area of the composite.

The photocatalytic activities of gaseous toluene over different CIS-BWO samples were evaluated under visible light irradiation, as shown in Fig. 5a. In the absence of catalysts, the photolysis efficiency of toluene was just 18% under visible light irradiation after 5 h. The conversion efficiencies of toluene were about 28%, 52%, 63% and 55% over BWO, 0.1%CIS-BWO, 1%CIS-BWO and 3%CIS-BWO, respectively. It is observed that the photocatalytic ability of 1%CIS-BWO is much higher than that of the pristine BWO. The kinetic data of gaseous toluene conversion reaction fit to a pseudo-first-order model, as expressed by $\ln(C_0/C_t) = kt$, where C_0 and C_t represent the concentrations of toluene before and after irradiation, t is irradiation time and k is the rate

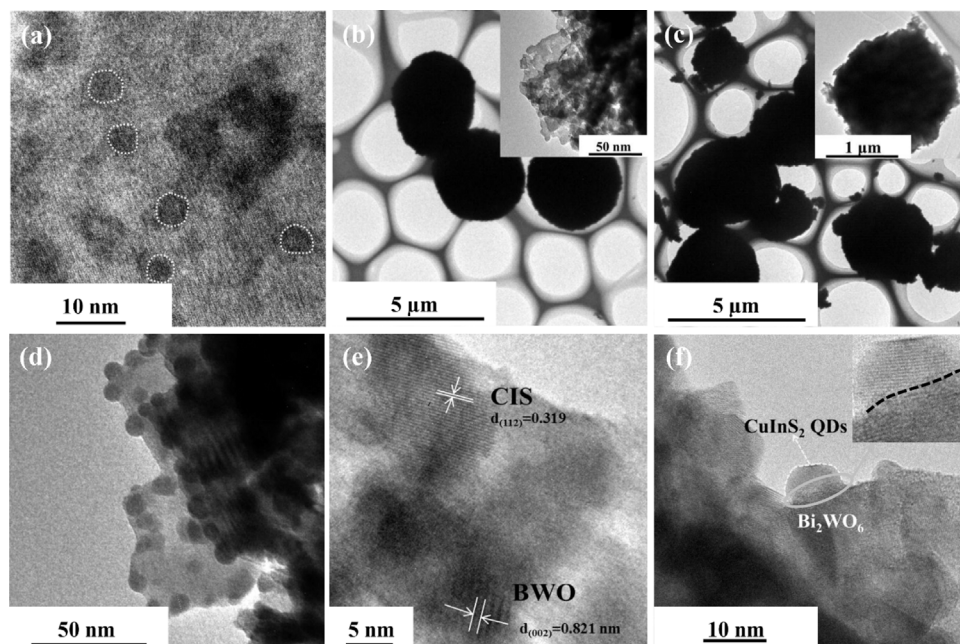**Fig. 2.** XRD patterns of the as-prepared samples.

Fig. 3. Typical TEM images of CIS-QDs (a), pristine BWO (b), 1%CIS-BWO (c and d), and HRTEM images of 1%CIS-BWO (e and f).

constant. The *k* values of the pristine BWO, 0.1%CIS-BWO, 1%CIS-BWO, and 3%CIS-BWO were 4.22, 6.05, 12.85 and 11.37 h^{-1}, respectively (in Fig. S3). In addition, as shown in Fig. 5b, the amount of CO_2 liberation over CIS-BWO heterojunctions were higher than that of pure BWO, and the order of CO_2 production over different CIS-BWO samples was consistent with that of toluene conversion efficiency, indicating that toluene was mineralized into CO_2. The above results demonstrate that after coupling with CIS-QDs, the photocatalytic activities and reaction rates of various CIS-BWO samples were efficiently improved by comparison with the pure BWO. These results demonstrate that the formation of heterojunction improves the transfer efficiency of charge carriers and simultaneously suppresses the recombination rate of photogenerated electron-hole pairs.

Furthermore, *in-situ* FTIR spectra as a useful tool were used to investigate the degradation procedure of gaseous toluene over 1%CIS-BWO sample, as displayed in Fig. S4. The apparent vibration at 3076 and 3040 cm^{-1} were assigned to C–H stretching vibration of benzene ring, and the absorptive peaks at 2938 and 2880 cm^{-1} were ascribed to C–H stretching vibration of methyl in toluene molecules [40,41]. Meanwhile, it was observed that the intensity of the characteristic peak of toluene gradually decreased, and the peaks intensity assigned to CO_2 (2325 and 2360 cm^{-1}) increased, demonstrating that toluene was converted to CO_2 and H_2O [42]. More importantly, the bands at 3750, 1700, and 3650 cm^{-1} belonging to surface benzyl alcohol, benzaldahyde, and benzoic acid were detected with the extension of irradiation time [43,44], as shown in Fig. S5, which illustrates that the
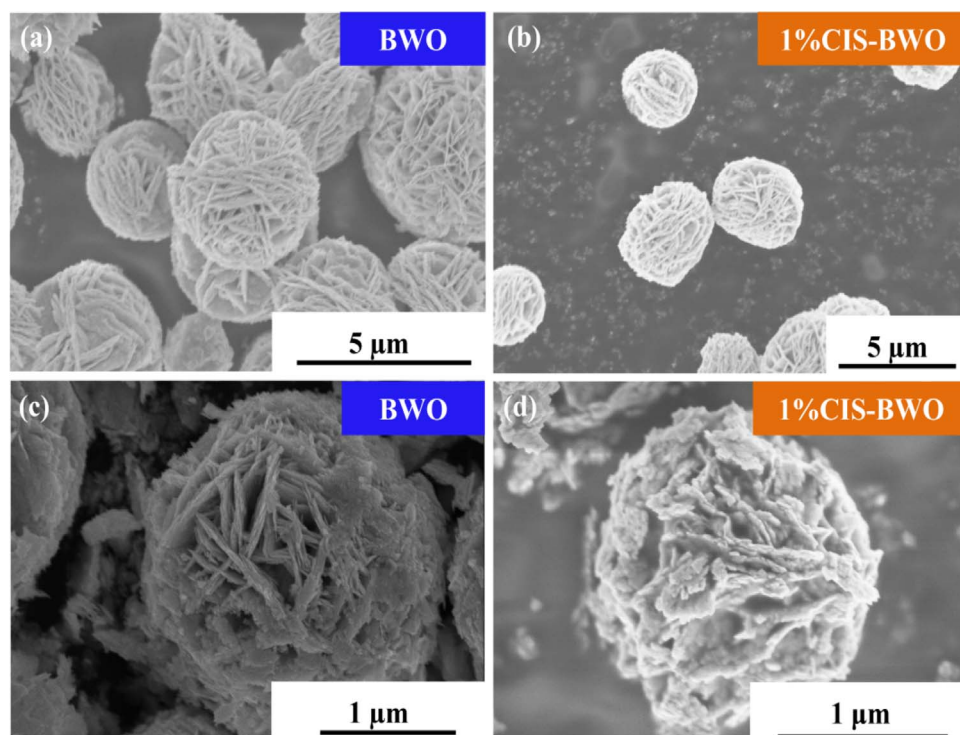

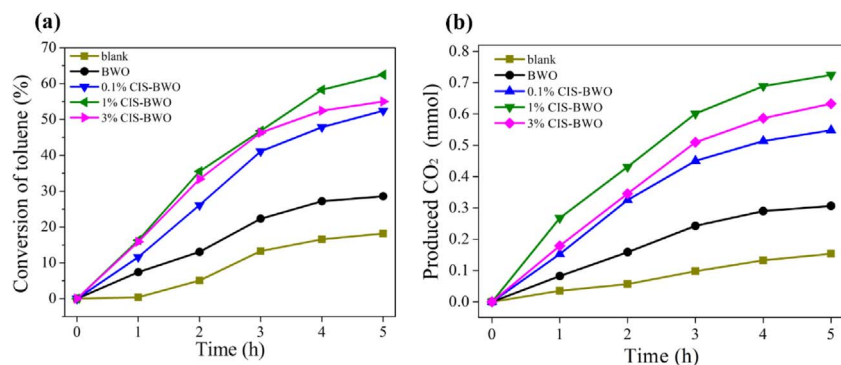**Fig. 4.** Typical SEM images of pure BWO (a and c) and 1%CIS-BWO (b and d).

photocatalytic oxidation reaction firstly occurred at the methyl of toluene. With the prolonging of irradiation time, the ratio of the C−H vibration intensity of aromatic ring to the C−H vibration intensity of methyl decreased gradually, which indicates that the aromatic ring was damaged after the oxidation of methyl of toluene.

Moreover, aqueous photoreduction of Cr(VI) over the as-prepared CIS-BWO heterojunctions under visible light irradiation were also carried out, as displayed in Fig. 6. In the blank test, the concentration of Cr(VI) remained unchanged under visible light illumination for 5 h, thus excluding the photolysis effect in the photoreduction of Cr(VI). When the CIS-BWO heterojunction samples were added, remarkable reduction of Cr(VI) was observed in Fig. 6a. The Cr(VI) photoreduction efficiencies in 5 h are about 10, 30, 60 and 90% on those catalysts in an order of 1%CIS-BWO > 3%CIS-BWO > 0.1%CIS-BWO > BWO, which is consistent with that of toluene oxidization. These results demonstrate that the formation of CIS-BWO heterojunction is beneficial for improving the photooxidative and photoreductive activities.

In addition, recycling experiments of Cr(VI) photoreduction over 1%CIS-BWO sample were conducted to investigate the stability of the photocatalyst. As presented in Fig. 6b, the 1%CIS-BWO sample retained good Cr(VI) photoreduction efficiency after four cycles and displayed a favorable stability. Furthermore, the 1%CIS-BWO sample after photocatalysis (CIS-BWO-AP) was investigated by TEM, XRD and XPS analyses. As displayed in Fig. S6a, the CIS-QDs still adhered on the surface of BWO compactly. The XRD pattern of CIS-BWO-AP exhibited good crystallinity and the distinct diffraction peaks were indexed to the orthorhombic Bi_2WO_6 phase (JCPDS No. 73-1126). The XPS spectra of the six elements (Cu, In, S, Bi, W and O) constituting the CIS-BWO-AP sample were in good accordance with those reported for $CuInS_2$ and Bi_2WO_6 (Fig. S6b-h) [45,46]. The above results confirmed that the heterojunctions possessed good physical and chemical stabilities.

To reveal the generation and separation of photogenerated charges in the heterojunction systems, the photoelectrochemical properties of the samples were investigated. Fig. 7a exhibits the transient photocurrent of the as-prepared samples, which produced a clear current response with on-off irradiation. It was observed that the pristine BWO produced a weak current density of ca. 0.1 nA/cm², while the 3%CIS-

BWO, 1%CIS-BWO, and 0.1%CIS-BWO samplers enlarged the current density to ca. 5 nA/cm², ca. 20 nA/cm², and ca. 1 nA/cm², respectively. Moreover, electrochemical impedance spectra (EIS), in general, were used to describe transportation process of the photoexcited electron/hole pairs, where a smaller arc radius indicates a higher efficiency in charge transfer [47].

In Fig. 7b, it was found that the CIS-BWO heterojunctions possess the smaller arc radius in comparison with the pristine BWO, which indicates that the CIS-BWO heterojunction system has the faster interfacial charge transfer. The lifetime of the injected electrons (τ) $\approx 1/(2\pi f)$ can be obtained from the electrochemical impedance spectra, where the life time of photogenerated electrons is inversely proportional to the characteristic frequency [48]. As shown in Fig. S7, the CIS-BWO heterojunction system has a longer electron lifetime and enhanced performance in transferring photoinduced charge carriers. In Fig. 7c, the heterojunction composites exhibit a lower emission intensity than that of pure BWO, indicating the decrease of charge irradiative recombination of the CIS-BWO heterojunction system. In Fig. 7d and Table S1, the PL decay of 1%CIS-BWO sample shows longer average lifetime of electrons than that of pure BWO, which demonstrates that the formation of heterojunction is beneficial for prolonging the lifetime of the photogenerated electrons. The above results indicate that the generation, separation, and transferring efficiency of photoinduced electron/hole pairs in the CIS-BWO heterojunction are significantly improved. In addition, as contrast experiment, a CIS-BWO-Mix sample prepared by mechanical mixing method was tested by the above-mentioned experiments. The photocatalytic performance of the CIS-BWO-Mix sample is weaker than the CIS-BWO heterojunction system (Fig. S8), which indicates that the formation of heterojunction could be beneficial for transportation of photoinduced charge carrier between the adjacent components, thus improving the separation efficiency of the heterojunction system.

To deeply unravel the interactions between CIS and BWO, the interface properties of the heterojunction system were explored. In Fig. 8a, a new characteristic Raman peak at 234 cm^{-1} assigned to Bi−S bond is observed in the CIS-BWO heterojunction system [49], while the Raman characteristic peak was not found in the pristine BWO and CIS-
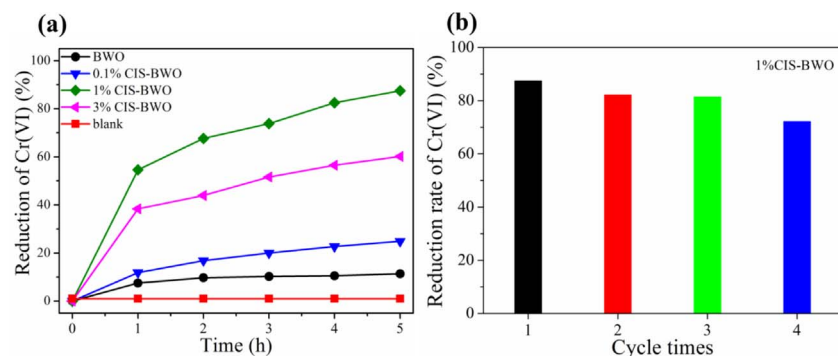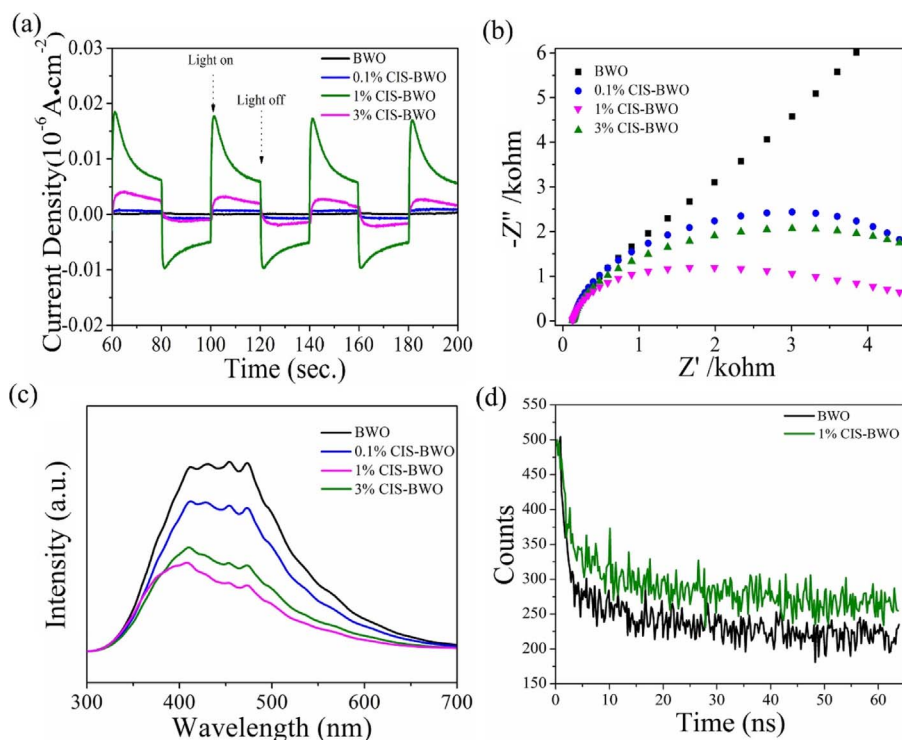
BWO-Mix samples. In addition, the FTIR spectra also validated the existence of the Bi−S bond in the CIS-BWO heterojunction samples, as displayed in Fig. 8b. Furthermore, as shown in Fig. 8c, the high resolution XPS spectra of Bi 4f in the CIS-BWO heterojunction displayed the obvious shoulder peaks at 158.2 and 163.5 eV attributing to the Bi−S bond, while the peaks were absent in the CIS-BWO-Mix sample, which further confirms the existence of Bi−S bond in the heterojuntion system [50]. In Fig. 8d, two peaks at 224.5 and 225.3 eV were ascribed to the sulfur atoms combined with the bismuth atoms in the CIS-BWO heterojunction and coordinated to Cu atoms in CIS-QDs, respectively [51,52]. In addition, the peak at 226.2 eV is originated from the thiol function group from the surface ligand [53]. Based on the above results, owing to the strong affinity between Bi^{3+} and S^{2-}, Bi−S bond at the interface between BWO and CIS-QDs formed during the calcination process (Fig. 8e and f).

The UV–vis diffuse reflection spectra of the prepared samples are displayed in Fig. 9a, which exhibits that the absorption edge of pure BWO is at 456 nm nearby the visible light region, whereas the photoresponse range of CIS-BWO was extended to the visible light range with the increasing of CIS-QDs content. The optical band gap energy can be estimated from the Kubelka-Munk formula and the band gaps of BWO, 0.1%CIS-BWO, 1%CIS-BWO, and 3%CIS-BWO were calculated to be about 2.72, 2.60, 2.51, and 2.40 eV, respectively, which suggests that the construction of the CIS-BWO heterojunctions could enhance the visible light response of the photocatalysts. Furthermore, the Mott-Schottky (M-S) analysis is the relationship between the space charge layer capacitance and the applied potential, utilized to calculate the flat band of photocatalysts [54].

$$\frac{1}{C^2} = \left(\frac{2}{\varepsilon \varepsilon_0 NA^2}\right)\left(E - E_{FB} - \frac{kT}{e}\right)$$

(1)

Here, C is the capacitance of the space charge layer, e is the elementary charge, ε is the dieletric constant of the semiconductor, $\varepsilon 0$ is the permittivity, A is the surface area, N is the carrier concentration, E is the applied potential, E_{FB} is the flat band potential, k is the Boltzmann constant, and T is the temperature. The M-S analysis allows for determining E_{FB} by extrapolating to the intercept of the potential axis.

Meanwhile, the slope (negative or positive) of the M-S plots provides information on the carrier type. It can be seen that the M-S plot of BWO shows a positive slope, which indicates the behavior of *n*-type semiconductor under depletion conditions [55], and $E_{FB} \approx -0.89$ eV *vs.* SCE, as shown in Fig. 9b. Meanwhile, the CIS-QDs displays a *p*-type semiconductor due to the negative slope and $E_{FB} \approx 0.51$ eV *vs.* SCE in the inset of Fig. 9b, which is in good agreement with the previous report [56]. In general, the flat band potential of a semiconductor is equal to its Fermi level, where the bottom of the conduction band (CB) of *n*-type semiconductor is more negative (about 0.2 eV) than Fermi level and the top of the valence band (VB) of *p*-type semiconductor is more positive (about 0.2 eV) than Fermi level. Therefore, the E_{CB} of BWO and the E_{VB} of CIS are −0.85 and 0.95 eV *vs.* NHE, respectively. Accordingly, based on the empirical formula ($E_g = E_{VB}-E_{CB}$), the E_{VB} of BWO and the E_{CB} of CIS are 1.87 and −1.03 eV *vs.* NHE, respectively.

Accompanying with the formation of heterojunction, the energy levels of CIS-QDs shifted upward, whereas the energy band of BWO shifted downward until the E_{FB} levels of CIS and BWO reached a thermodynamic equilibrium [57]. Upon the thermodynamic equilibrium, the two photocatalysts have a uniform Fermi level, as presented in Fig. 10. At that time, the different values (*D*-values) between the conduction band bottom of BWO and that of CIS, as well as the *D*-values between the valence band top of BWO and that of CIS became larger. Forced by the expanding potential *D*-values and the inner electrical fields (IEF) in the interfaces, the excited electrons in the CB of CIS migrated to that of BWO easily through Bi−S bonds, while the excited holes in the VB of BWO transferred to that of CIS. As a result, such Bi−S bonds connecting *p-n* CIS-BWO heterojunctions promote the separation of photo-generated charge carriers and inhibit the recombination of electron/hole pairs, thus enhancing the photocatalytic activity.

4. Conclusions

A novel *p-n* heterojunction has been synthesized through a facile and low temperature thermal treatment. After introducing CIS-QDs into the BWO, a useful Bi−S bond was found between CIS-QDs and BWO, resulting in the formation of CIS-BWO heterojunction. The obtained CIS-BWO heterojunction system displayed enhanced photocatalytic
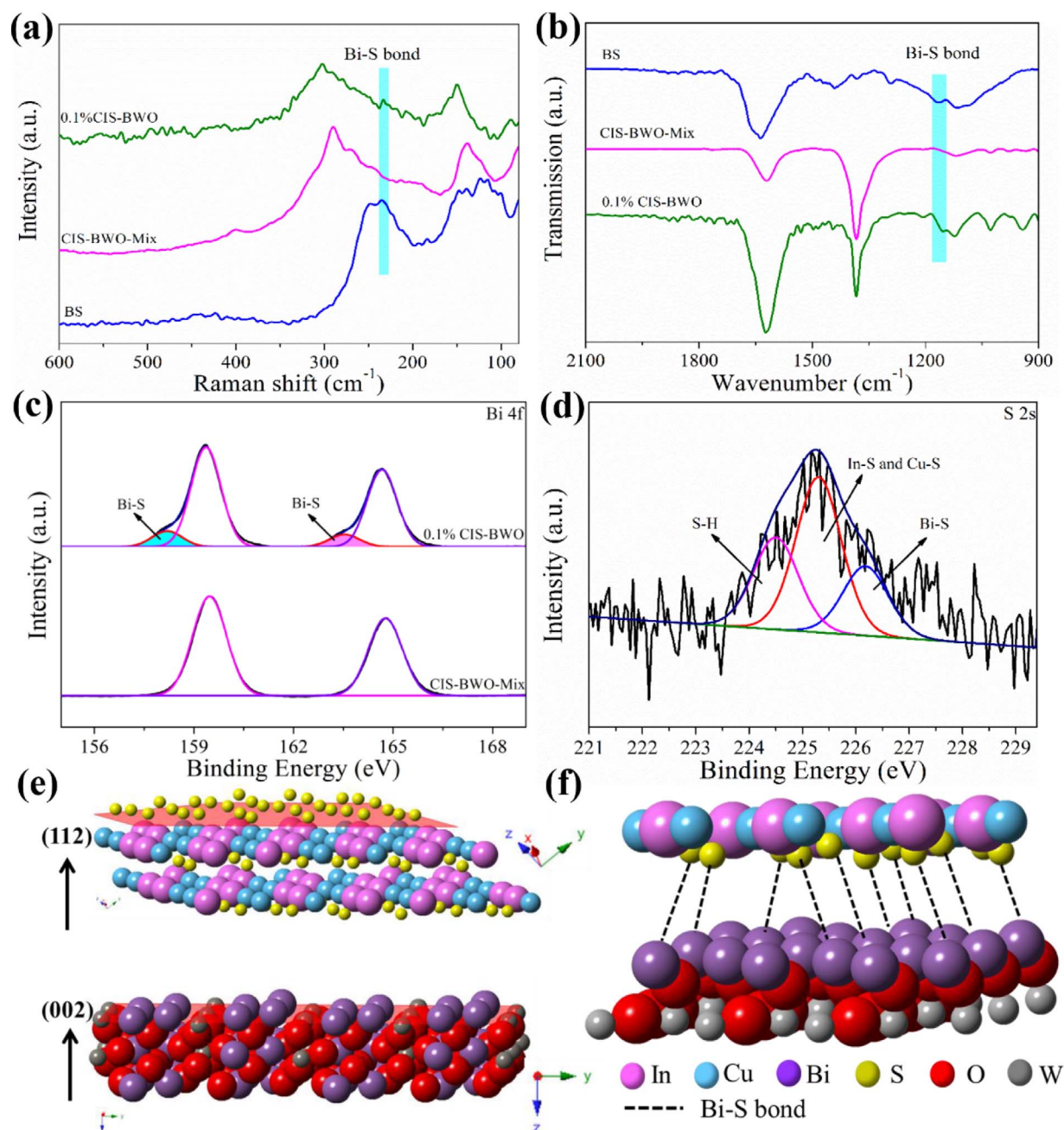
Fig. 8. Raman spectra (a), FTIR curves (b), high resolution XPS spectra of Bi 4f (c) and S 2 s (d) of the as-prepared samples, the unit cell of BWO and CIS (e), and schematic illustration of CIS-BWO joining *via* Bi−S s (f).
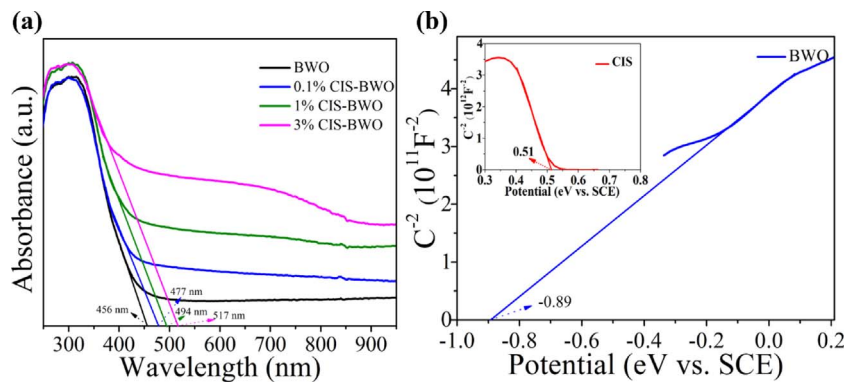

Fig. 9. UV–vis diffuse reflectance spectra of the as-prepared samples (a) and Mott-Schottky plots for BWO and CIS (b).
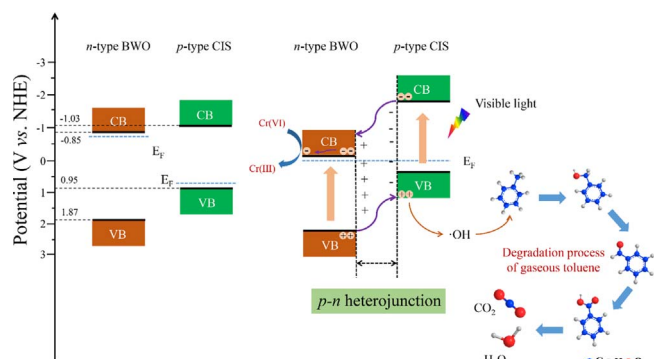
Fig. 10. Schematic diagram of formation of *p-n* heterojunction and proposed charge separation process.

performance for oxidizing toluene and reducing Cr(VI) by compared with the pristine BWO and CIS-BWO-Mix samples under visible light irradiation. Moreover, the photoelectrochemical characterizations show the enhanced transportation and increased electron lifetime after the formation of the *p-n* heterojunction and Bi−S s, which exert a positive impact on the harvesting efficiency of solar energy and reducing the transportation barrier of charge carrier inside the *n-p* heterojunction system. This work not only provides a new path for improving the photocatalytic activity of developed photocatalysts, but also offers a novel design and preparation of other high performance heterojunction nanomaterials for photocatalytic applications, such as water splitting, CO_2 reduction, and solar cells.

Acknowledgments

Appendix A. Supplementary data

Supplementary data associated with this article can be found, in the online version, at http://dx.doi.org/10.1016/j.apcatb.2017.09.028.

References

[1] P. Fu, K. Kawamura, J. Chen, Y. Miyazak, Environ. Sci. Technol. 48 (2014) 8491–8497.
[2] Y. Liu, M. Shao, W. Kuster, P. Goldan, X. Li, S. Lu, J.A. De Gouw, Environ. Sci. Technol. 43 (2009) 75–81.
[3] P. Yang, Z. Shi, S. Yang, R. Zhou, Chem. Eng. J. 126 (2015) 361–369.
[4] A. Ikhlaq, B. Kasprzyk-Hordern, Appl. Catal. B: Environ. 200 (2017) 274–282.
[5] F. He, J. Luo, S. Liu, Chem. Eng. J. 294 (2016) 362–370.
[6] M.S. Kamal, S. Razzak, M. Hossain, Atoms Environ. 140 (2016) 117–134.
[7] J. Kou, C. Lu, J. Wang, Y. Chen, Z. Xu, R. Varma, Chem. Rev. 117 (2017) 1445–1514.
[8] R. Monteiro, S. Miranda, C. Rodrigues-Silva, J. Faria, A. Silva, R. Boaventura, V. Vilar, Appl. Catal. B: Environ. 165 (2016) 306–315.
[9] B. Bajorowicz, J. Nadolna, W. Lisowski, T. Klimczuk, A. Zaleska-Medynska, Appl. Catal. B: Environ. 203 (2017) 452–464.
[10] L. Ma, S. Liang, X. Liu, D. Yang, L. Zhou, Q. Wang, Adv. Funct. Mater. 25 (2015) 898–904.
[11] N. Zhang, R. Ciriminna, M. Pagliaro, Y. Xu, Chem. Soc. Rev. 43 (2014) 5276–5287.
[12] T. Saison, P. Gras, N. Chemin, C. Chaneac, O. Duruphty, V. Brezova, C. Colbeau-Justin, J. Jolivet, J. Phys. Chem. C 117 (2013) 22656–22666.
[13] S. Murcia, K. Villa, T. Andreu, J. Morante, ACS Catal. 4 (2014) 3013–3019.
[14] L. Zhang, D. Bahnemann, ChemSusChem 6 (2013) 283–290.
[15] X. Ding, K. Zhan, L. Zhang, Environ. Sci. Technol. 48 (2014) 5823–5831.
[16] P. Chen, L. Zhu, S. Fang, C. Wang, G. Shan, Environ. Sci. Technol. 46 (2012) 2345–2351.
[17] H. Li, Y. Zhou, W. Tu, J. Ye, Z. Zou, Adv. Funct. Mater. 25 (2015) 998–1013.
[18] H. Wang, L. Zhang, Z. Chen, J. Hu, S. Li, Z. Wang, J. Liu, X. Wang, Chem. Soc. Rev. 43 (2014) 5234–5244.
[19] F. Meng, J. Li, S. Cushing, M. Zhi, N. Wu, J. Am. Chem. Soc. 135 (2013) 10286–10289.
[20] S. Kersha, L. Jing, X. Huang, M. Gao, A. Rogach, Mater. Horiz. 4 (2017) 155–205.
[21] M. Han, W. Chen, H. Guo, L. Yu, B. Li, J. Jia, J. Power Sources 318 (2016) 121–127.
[22] J. Ke, X. Li, Q. Zhao, B. Liu, S. Liu, S. Wang, J. Colloid Interface Sci. 496 (2017) 425–433.
[23] X. Hu, Y. Li, J. Tian, H. Yang, H. Cui, J. Ind. Eng. Chem. 45 (2017) 189–196.
[24] W. Cui, W. An, L. Liu, J. Hu, Y. Liang, J. Hazard. Mater. 280 (2014) 417–427.
[25] S. Wang, S. Kershaw, G. Li, M. Leung, J. Mater. Chem. C 3 (2015) 3280–3285.
[26] L. Li, A. Pandey, D. Werder, B. Khanal, J. Pietryga, V. Klimov, J. Am. Chem. Soc. 133 (2011) 1176–1179.
[27] H. Zhong, S. Lo, T. Mirkovic, Y. Li, Y. Ding, Y. Li, G. Scholes, ACS Nano 9 (2010) 5253–5262.
[28] Y. Yang, W. Que, X. Zhang, Y. Xing, X. Yin, Y. Du, J. Hazard. Mater. 317 (2016) 430–439.
[29] H. Zhong, Y. Zhou, M. Ye, Y. He, J. Ye, C. He, C. Yang, Y. Li, Chem. Mater. 20 (2008) 6434–6443.
[30] R. Xie, M. Rutherford, X. Peng, J. Am. Chem. Soc. 131 (2009) 5691–5697.
[31] M. Booth, A. Brown, S. Evans, K. Critchley, Chem. Mater. 24 (2012) 2064–2070.
[32] J. Park, Y. Nam, J. Colloid Interface Sci. 460 (2015) 173–180.
[33] Y. Zhou, Z. Tian, Z. Zhao, Q. Liu, J. Kou, X. Chen, J. Gao, S. Yan, Z. Zou, ACS Appl. Mater. Interfaces 3 (2011) 3594–3601.
[34] Y. Zhang, N. Zhang, Z. Tang, Y. Xu, Chem. Sci. 4 (2013) 1820–1824.
[35] L. Ge, J. Liu, Appl. Catal. B: Environ. 105 (2011) 289–297.
[36] J. Di, J. Xia, Y. Ge, H. Li, H. Ji, H. Xu, Q. Zhang, H. Li, M. Li, Appl. Catal. B: Environ. 168–169 (2015) 51–61.
[37] T. Li, Y. Lee, H. Teng, Energy Environ. Sci. 5 (2011) 5315–5324.
[38] S. Sun, W. Wang, L. Zhang, E. Gao, D. Jiang, Y. Sun, Y. Xie, ChemSusChem 6 (2013) 1873–1877.
[39] G. Li, F. Qin, H. Yang, Z. Lu, H. Sun, R. Chen, Eur. J. Inorg. Chem. 18 (2012) 2508–2513.
[40] J. Sun, X. Li, Q. Zhao, M. Tade, S. Liu, J. Mater. Chem. A 3 (2015) 21655–21663.
[41] J. Liu, X. Li, Q. Zhao, J. Ke, H. Xiao, X. Lv, S. Liu, M. Tade, S. Wang, Appl. Catal. B: Environ. 200 (2017) 297–308.
[42] D. Selishchev, N. Kolobov, A. Pershin, D. Kozlov, Appl. Catal. B: Environ. 200 (2017) 503–513.
[43] J. Sun, X. Li, Q. Zhao, J. Ke, D. Zhang, J. Phys. Chem. C 118 (2014) 10113–10121.
[44] F. Zhang, M. Wang, X. Zhu, B. Hong, W. Wang, Z. Qi, W. Xie, J. Ding, J. Bao, S. Sun, C. Gao, Appl. Catal. B: Environ. 170–171 (2015) 215–224.
[45] H. Huang, K. Liu, K. Chen, Y. Zhang, Y. Zhang, S. Wang, J. Phys. Chem. C 118 (2014) 14379–14387.
[46] C. Ye, M. Regulacio, S. Lim, Q. Xu, M. Han, Chem. Eur. J. 18 (2012) 11258–11263.
[47] X. Wang, J. Xie, C. Li, J. Mater. Chem. A 3 (2015) 1235–1242.
[48] G. Natu, P. Hasin, Z. Huang, Z. Ji, M. He, Y. Wu, ACS Appl. Mater. Interfaces 4 (2012) 5922–5929.
[49] J. Ota, S. Srivastava, J. Phys. Chem. C 111 (2007) 12260–12264.
[50] Y. Pei, X. Li, H. Chu, Y. Ge, P. Dong, R. Baines, L. Pei, M. Ye, J. Shen, Talanta 165 (2017) 44051.
[51] Y. Bhoi, B. Mishra, Chem. Eng. J. 316 (2017) 70–81.
[52] M. Han, J. Jia, L. Yu, G. Yi, RSC Adv. 5 (2015) 51493–51500.
[53] P. Schaal, A. Besmehn, E. Maynicke, M. Noyong, B. Beschoten, U. Simon, Langmuir 28 (2012) 2448–2454.
[54] J. Ke, J. Liu, H. Sun, H. Zhang, X. Duan, P. Liang, X. Li, M. Tade, S. Liu, S. Wang, Appl. Catal. B: Environ. 200 (2017) 47–55.
[55] M. Li, L. Zhang, X. Fan, Y. Zhou, M. Wu, J. Shi, J. Mater. Chem. A 3 (2015) 5189–5196.
[56] D. Jara, S. Yoon, K. Stamplecoskie, P. Kamat, Chem. Mater. 26 (2014) 7221–7228.
[57] Y. Peng, M. Yan, Q. Chen, C. Fan, H. Zhou, A. Xu, J. Mater. Chem. A 2 (2014) 8517–8524.